Nanoscale

ROYAL SOCIETY OF CHEMISTRY

COMMUNICATION

View Article Online
View Journal | View Issue

Cite this: *Nanoscale*, 2022, **14**, 1706

Received 10th November 2021,
Accepted 19th December 2021

DOI: 10.1039/d1nr07455e

rsc.li/nanoscale

Deep X-ray lithography on "sol–gel" processed noble metal mesoarchitectured films†

Maxime Gayrard,[a] Benedetta Marmiroli,[b] Francois Chancerel,[a,c,d] Philippe Decorse,[e] Heinz Amenitsch,[b] Jennifer Peron,[e] Andrea Cattoni[c,d] and Marco Faustini *[a]

Noble metal coordination xerogel films (mesostructured with block-copolymers) exhibit solubility switching with increasing X-ray irradiation. Different from other sol–gel systems, these are attributed to film deconstruction under irradiation. These materials can be used as recyclable negative tone resists for deep X-ray lithography that can be further converted into metallic nanoarchitectured films.

[a]*Sorbonne Université, CNRS, Laboratoire Chimie de la Matière Condensée de Paris (LCMCP), F-75005 Paris, France. E-mail: marco.faustini@sorbonne-universite.fr*
[b]*Institute of Inorganic Chemistry, Graz University of Technology, Graz, Austria*
[c]*Institut Photovoltaïque d'Ile-de-France (IPVF), CNRS UMR 9006, Palaiseau, France*
[d]*Centre de Nanosciences et de Nanotechnologies (C2N), CNRS UMR 9001, Université Paris-Saclay, Palaiseau, France*
[e]*Université de Paris, ITODYS, CNRS, UMR 7086, 15 rue J-A de Baïf, F-75013 Paris, France*

†Electronic supplementary information (ESI) available. See DOI: 10.1039/d1nr07455e

Marco Faustini

Dr. Marco Faustini was trained as a materials engineer at the University of Trento (Italy) and Aalto University (Finland). He obtained his PhD at Université Pierre et Marie Curie (France) working on the self-assembly of sol–gel based magnetic nanomaterials for data storage. He then carried out a postdoctoral stay at POSTECH (South Korea) working on the microfluidic synthesis of MOFs. Since 2012, he has served as an Associate Professor at Sorbonne University (Paris). His research interests lie in the field of synthesis and processing of porous materials by colloidal self-assembly and nanolithography. The main applications are in the fields of electrocatalysis and photonics.

Metallic nano- and microstructured films play a key role in the development of devices in a number of fields including electronics,[1,2] photonics,[3] microfluidics,[4] electrochemistry[5] or (photo) catalysis.[6] Their integration into devices requires the development of a patterning strategy of the metallic materials. Among them, gold and silver (or even cheaper aluminum) have been widely explored. However, other noble metals (such as those of the platinum group) are of particular interest because of their superior thermal and chemical stability, opening perspectives in emerging applications.[7] In electronics, metallic ruthenium films are used as barriers for future generation metal interconnects in logic devices and as metal electrodes for DRAM capacitors.[8,9] Rhodium has recently gained attention in the field of ultraviolet (UV) plasmonics as an O_2-resistant plasmonic photocatalyst.[10] Despite that, patterning strategies enabling integration into devices have not been reported (for Rh) or they require multi-step processes (for Ru).[1] In addition, conventional processes are indirect and rely on the patterning of a sacrificial resist (polymer) followed by lift-off, electrodeposition and/or etching processes that can be very demanding for stable noble metals. Developing scalable and direct patterning strategies for noble metals would greatly simplify their integration into a number of devices. Besides polymeric resists, direct patterning has already been demonstrated for metal–organic frameworks[11–14] and mesoporous oxides prepared by a sol–gel process.[15–17] Among various techniques, deep X-ray lithography has proven to be very effective for the direct patterning of sol–gel precursors that have been used as negative tone resists and further converted into oxides, typically by annealing.[17–20] For instance, X-ray patterned Ti-based xerogels could be converted into crystalline TiO_2 by a thermal treatment.[18] Generalizing the concept of the "sol–gel process" beyond oxides by extending it to noble metals would enable the direct patterning of metallic structures by X-ray lithography. To do so, one must develop noble metal-based resists with two main requirements: (i) the resist should exhibit a solubility switch upon X-ray exposure to allow for development; and (ii) the resist should be directly converted into metals by annealing. In addition, considering the high cost of noble

metal precursors, the process should be waste-free and should ideally allow for the recycling of the expensive resist using environmentally friendly solvents (such as H_2O). Here we show that mesostructured xerogels based on Ru and Rh (in the presence of block-copolymers) act as effective negative tone resists for X-ray lithography to obtain metallic nanostructures after annealing. Different from previous reports on sol–gel derived transition metal oxides, we report for the first time on the radiation chemistry of the underexplored "sol–gel" of noble metals. The key advantage of this "sol–gel" approach is that the materials can be shaped as polymeric resists by solution processing but can eventually be converted into metals. The general patterning strategy for noble metal xerogels is illustrated in Fig. 1(a). Resist films are obtained from solutions containing noble metal precursors (chlorides) and the block-copolymer Pluronic F127. Different from other noble metal chlorides such as gold, silver, platinum or palladium (that recrystallize after evaporation), in the presence of block-copolymers, Ru or Rh chlorides form homogeneous films of optical quality after dip-coating (Fig. S1†). The dip-coating method is a waste-free deposition technique, an important feature in the case of costly noble metal precursors.[21] The film is then exposed to synchrotron X-ray radiation through a mask that induces a solubility change; the exposed materials become insoluble in polar solvents. The non-exposed material is developed in water. Water is also one of the solvents of the initial solution, and this is a key condition for recycling the initial noble metal precursors. The patterned insoluble materials can be annealed under a reducing atmosphere (H_2 at 300 °C) and can be directly converted into the corresponding noble metal.

A detailed study on the structural and chemical evolution of the materials induced by X-ray exposure is presented for the Ru-based films. We first discuss the evolution of the structure. As in the classical sol–gel process, self-assembly during evaporation (during the dip-coating step) results in the formation of mesostructured hybrid materials that are composed of organic micelles surrounded by amorphous metallic complexes.[16] This was confirmed by GISAXS on a $RuCl_3$/F127 film before exposure (Fig. 1e). The GISAXS measurement of the non-exposed material shows the characteristic diffraction pattern of the *Im3m* mesostructure (body centered cubic arrangement).[17] After X-ray exposure, in all of the cases, a colour difference between the exposed and unexposed zones (latent image) is already visible to the naked eye as exemplified in the optical photograph in Fig. 1(b). The colour difference can be attributed to a structural modification of the films (such as a decrease in the thickness). We thus investigated in detail the effect of the X-ray radiation dose on the structural properties of the films by UV-visible spectroscopic ellipsometry and GISAXS. The evolution of the relative thickness *vs.* dose is shown in Fig. 1(c). For all of the films investigated hereafter, the initial thickness was around 100 nm. The relative thickness decreased significantly at low doses and progressively reached a contraction of 66% at higher doses. This decrease in thickness is characteristic of the densification of the material due to X-ray radiation. Densification can be due to water loss and/or polymer degradation. The same study was performed for $RuCl_3$ films without F127 (Fig. S2†) and at moderate exposure doses, the $RuCl_3$ films exhibited a contraction of 30%–33%. This decrease can therefore be attributed to the partial loss of adsorbed water (more details will be shown later

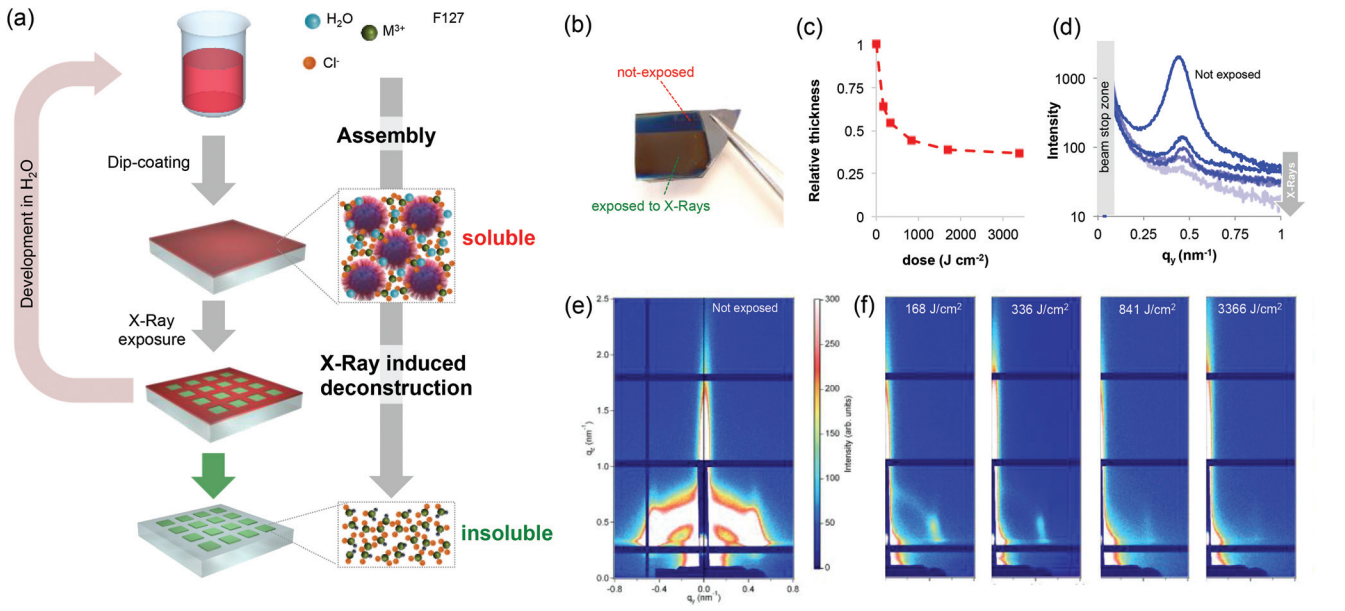

Fig. 1 (a) Illustration of the patterning strategy of noble metal mesostructured xerogels. (b) Photograph of a Ru-based xerogel partially exposed to X-ray radiation. (c) Evolution of the relative thickness of a $RuCl_3$/F127 xerogel as a function of X-ray dose. (d) Evolution of the scattering intensity as a function of the *qy* for samples exposed to increasing doses. (e) GISAXS patterns of the unexposed $RuCl_3$/F127 xerogel and, (f) evolution of the GISAXS pattern of the sample at increasing exposure doses.

on). To gain a better understanding, the evolution of the mesostructure after increasing doses of exposure was investigated by GISAXS (Fig. 1f). The characteristic diffraction signal of the unexposed film progressively disappeared upon X-ray irradiation; we integrated the signal intensity along the in-plane 1–10 direction as a function of the X-ray dose (Fig. 1d). The diffraction signal at q_y = 0.42 nm^{-1} corresponds to a *d*-spacing of 14.9 nm, which is in agreement with mesostructures containing F127 micelles. The strong decrease of the intensity at low doses indicates a loss of the mesostructure, likely due to a chemical modification of the block-polymer micelles.[22]

The chemical evolution during exposure was investigated by (i) GIWAXS and XPS to characterize the noble metal precursors and (ii) infrared (IR) spectroscopic ellipsometry to probe the evolution of the polymer and H_2O. The chemical evolution of the inorganic precursors *vs.* X-ray irradiation was first characterized by GIWAXS. As shown in Fig. S3,† the GIWAXS patterns do not show any characteristic diffraction peaks indicating that the Ru-based xerogels are amorphous. To gain a better understanding, the evolution of the Ru, O and Cl oxidation states upon exposure was probed by XPS (Fig. 2a and Fig. S4†). Since Ru(3d) core levels superimpose the C(1s) core level, the Ru(3p) region was analyzed. From the plotted Ru(3p) spectra in Fig. 2(a), we can see that Ru(3p) does not shift upon exposure time and remains at 463.1 eV, which is characteristic of Ru(III) species. Interestingly, Cl/Ru ratio for the non-exposed sample was ~3 confirming that the film presents a stoichiometry close to the initial $RuCl_3$ precursor, which is in agreement with previous reports.[23,24] Before exposure, noble metal precursors, which can be formally described as $Ru(Cl)_x$ $(OH)_y$, are likely coordination xerogels based mostly on Cl ligands.[25] The characteristic peaks of Cl 2p3/2 and 2p1/2 also remain located at 197.8 and 199.3 eV upon exposure, respectively (Fig. S4†); however, a progressive decrease in the Cl/Ru ratio was observed as the exposure time increased. The Cl/Ru ratio decreased from ~3 for the non-exposed sample, down to 2.53, 1.46 and 0.71 with exposure doses of 168, 336 and 841 respectively. This decrease of the Cl content can be attributed to the formation of more hydroxylated species (–OH). The XPS spectra in the O 1s region (Fig. S4†) confirm the presence of H_2O in non-exposed samples with the O(1s) peak centered at 533 eV. Upon exposure, the contribution of water to the O(1s) peak disappears and the O(1s) peak is shifted to 531.5 eV which is characteristic of hydroxylated species. In contrast, no peaks centered at 529.3 eV, characteristic of the M–O–M bond, were observed.[23] This suggests that different from other sol–gel systems, X-ray irradiation does not promote condensation in the case of Ru.

We then performed IR ellipsometry as shown in Fig. 2(b). During the ellipsometric experiment, the IR polarized light beam interacted with the film. This interaction changes the polarization state of the reflected light which may be parametrized by the interference amplitude component Ψ and the phase difference Δ. Both values (Ψ and Δ) are very sensitive to photon absorptions due to the vibrational modes at IR wavelengths. The Ψ and Δ spectra were then analyzed using the software "IR Wase" to obtain the refractive index (n) and extinction coefficient (k) of the films. Fig. 2(b) shows the evolution of k as a function of wavelength for the Ru-based films before and after X-ray exposure. Before exposure, the $RuCl_3$/F127 film shows many different features: the bands centered between 1650 and 1670 cm^{-1}, and between 3200 and 3400 cm^{-1} can be attributed to the presence of water molecules in the film, due to residual water from the initial solution and/or humidity from the atmosphere.[26] The large O–H band between 3200 and 3400 cm^{-1} partially overlaps in the range of 2850–2920 cm^{-1} with the CH_2 symmetric and asymmetric stretching bands of Pluronic F127. The band at *ca.* 1100 cm^{-1} can be attributed to the stretching of the C–O–C bond in the PEO.[26,27] To confirm, the k spectra of the $RuCl_3$ and F127 films (non-exposed) are also reported in Fig. S5.† After exposure at a low dose of 168 J cm^{-2}, a drastic decrease of the O–H band confirms a partial water loss while the characteristic peaks of the polymers are not visible. At a high dose of 841 J cm^{-2}, the raw ellipsometry spectra do not present any

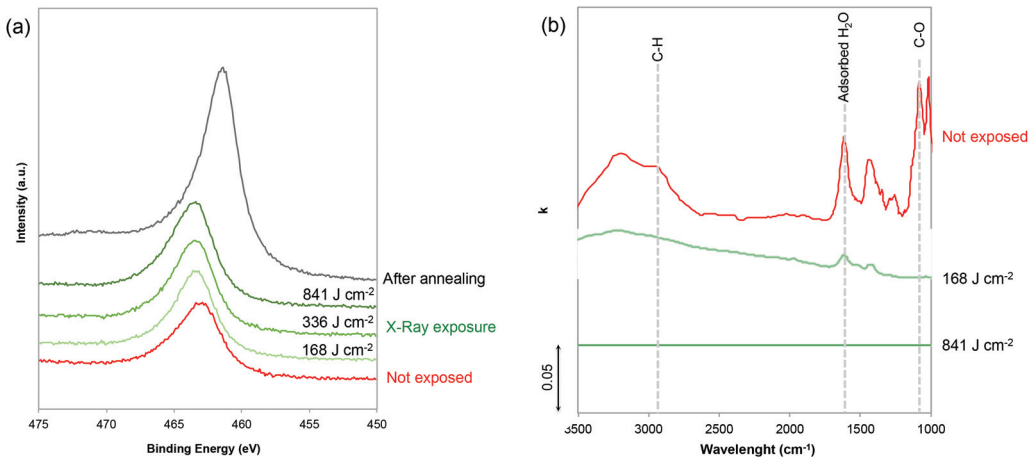

Fig. 2 (a) XPS spectra recorded in the Ru(3p) region on films exposed to different doses and annealed under a reducing atmosphere. (b) Evolution of the extinction coefficient k of a $RuCl_3$/F127 film before and after exposure at different doses.

visible absorption peaks and are thus fitted with a Cauchy model for not absorbing materials (k = 0). It is important to mention that the presence of the residual polymer or water might fall below the detection limit of the IR ellipsometer. However, it is reasonable to propose that X-ray irradiation induces the deconstruction of the film with two main effects: (i) a loss of the mesostructure (as observed by GISAXS) that can be attributed to the fact that high energy X-ray radiation provokes the complete decomposition of F127;[22] and (ii) the loss of the adsorbed water that is in agreement with the UV-vis ellipsometry analysis (Fig. S2†) and formation of hydroxocomplexes. What we observed in this study is in agreement with previous literature on sol–gel derived films.[28] The hard X-ray exposure to the as-deposited sol–gel films leads to the hydrolysis of the precursors that are promoted by the formation of the free radicals, $H^{\bullet}$ and $OH^{\bullet}$ which are formed by the dissociation of water molecules exposed to X-ray radiation. Residual water is indeed always present in the hybrid films containing F127 and hydrated noble metal precursors. Free radicals are also responsible for the decomposition of the organic matter in the films.[28]

Film deconstruction during X-ray exposure was also observed in the case of the $RhCl_3$ films templated with F127. Fig. 3 shows the evolution of relative thickness as a function of the dose. As observed for Ru, the Rh-based films contract progressively (up to 62% at high dose values), which is attributed to water loss and the decomposition of F127. The loss of the mesostructure was also confirmed by the selected GISAXS patterns shown in the inset of Fig. 3. The progressive decrease of the GISAXS signal is in agreement with the mechanism described for Ru-based films.

Coming back to the lithographic process, the combination of polymer decomposition, dehydration and partial hydroxylation is responsible for the solubility switch of the films. As mentioned above, to obtain an efficient negative tone resist for lithography, the exposed material must be insoluble while the unexposed material must be soluble. The solubility contrast is thus crucial for the development step. We have tested the effectiveness of the development process on samples patterned through a mask. Examples of the patterned samples before development are shown in Fig. S6.† The development step involved dipping the samples in H_2O for about 30 s; the quality of the micropatterns was then evaluated by optical microscopy. The table in Fig. 4(a) summarizes the results of the development for the two metal precursors Ru/Rh chlorides alone or in the presence of the block-copolymer (F127) as a function of the exposure dose. Several general trends were observed. For all of the systems, at low doses, the development is not efficient since the exposed material can be re-dissolved in H_2O. Whereas, for high doses (that implies a very long exposure time) the development is not optimal: overexposure also induces a modification in the unexposed material at the pattern edge that becomes less soluble after irradiation. Films made of $RuCl_3$ and $RhCl_3$ without F127 become insoluble after irradiation as well. This is not surprising since more hydroxylated Ru complexes present poor solubility in water.[29] However, without F127, the solubility contrast (between the exposed and unexposed zones) is not high enough to achieve effective development in H_2O. For the $RuCl_3$/F127 and $RhCl_3$/F127 materials, 841 J cm^{-2} is the optimal X-ray dose to obtain effective development under our conditions as exemplified in the optical micrographs in Fig. 4(b) and (c). Similarly, samples exposed at 841 J cm^{-2} were developed in other polar solvents such as ethanol (Fig. S7†). After development, the patterned noble metal xerogels were converted into the respective metals by annealing at 300 °C under a reducing atmosphere (H_2/Ar) as illustrated in Fig. 5(a). XPS analysis in Fig. 2(a) of the film after annealing shows a Ru(3p) signal, which is characteristic of a

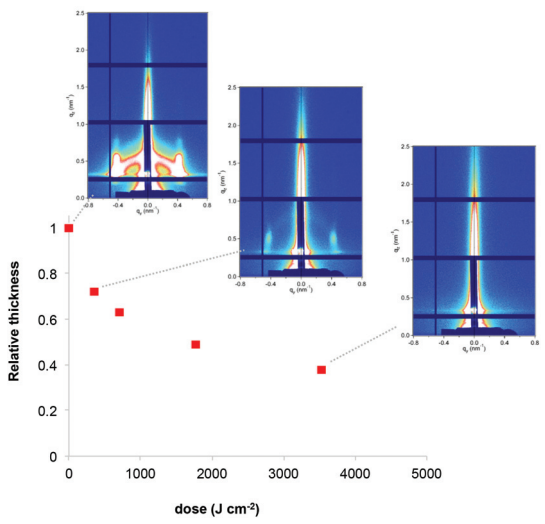

Fig. 3 Evolution of the relative thickness of the $RhCl_3$/F127 films as a function of X-ray dose. Inset: the corresponding GISAXS patterns.

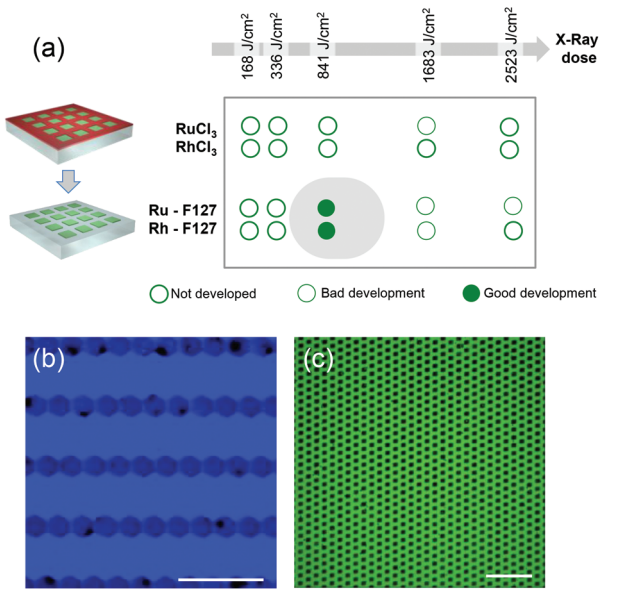

Fig. 4 (a) Summary of the results of the development for the two metal precursors Ru/Rh chlorides alone or in the presence of the block-copolymer (F127) as a function of exposure doses (b) and (c) false-colored optical micrographs of the developed Rh and Ru-based resists respectively (scale bar 100 μm).

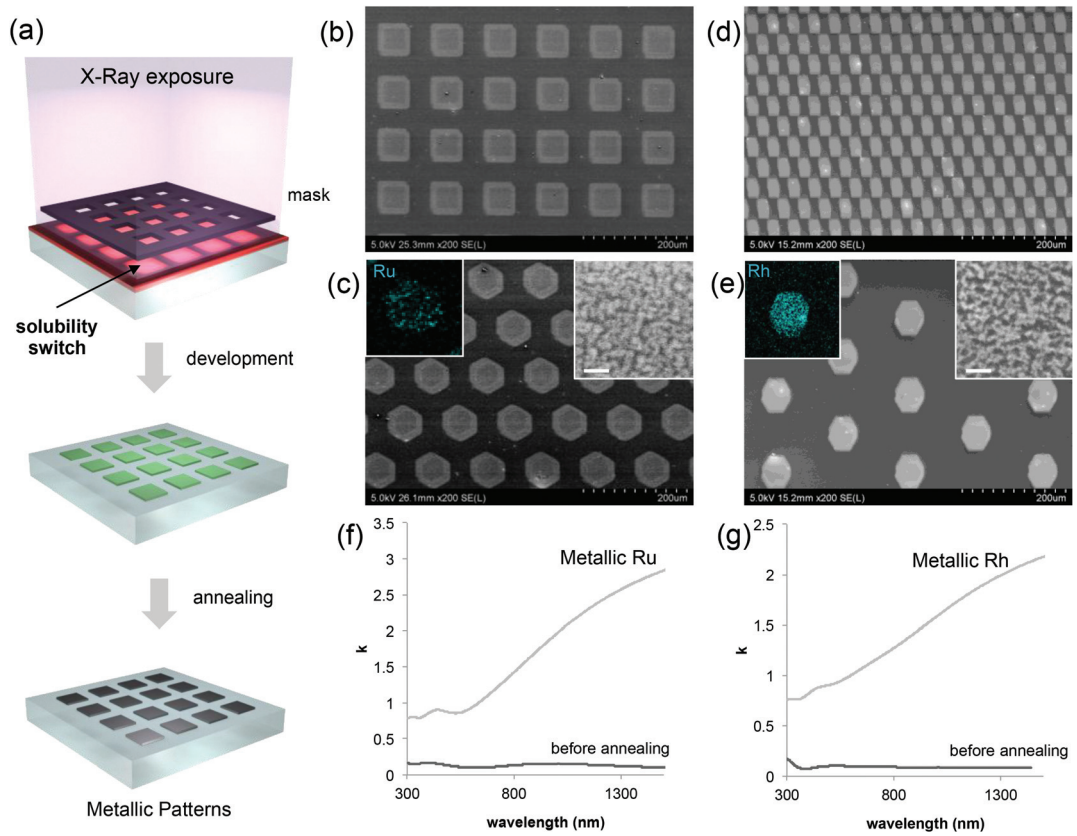

Fig. 5 (a) Illustration of the lithographic process toward metallic patterns; SEM micrographs of (b) and (c) Ru and (d) and (e) Rh patterns. The corresponding EDX mapping and higher resolution view are reported in the inset (scale bar 50 nm). (f) and (g) Evolution of the extinction coefficient *k* for Ru and Rh-samples before and after annealing.

Ru(0) species at 461.3 eV. SEM micrographs in Fig. 5(b)–(e) show some examples of micropatterned Ru and Rh films obtained after annealing and exposure at 841 J cm^{-2} on resists containing F127. A higher magnification SEM micrograph of the pattern's edge is shown in Fig. S8.† EDX mapping (insets of Fig. 5) on single features indicate that only the metal is present without significant presence of O, Cl or N atoms (not shown). SEM micrographs in the inset (Fig. 5c and d) show that metallic films fabricated by the sol–gel process are not dense but present porous nanoarchitectures. Indeed, during the reduction process, the Cl/OH ligands are decomposed resulting in films that are composed of metallic nanoparticles, which form a percolated network with voids. The formation of the percolated nanoparticle layers (rather than isolated particles) is important for ensuring the metallic properties of the films (electrical and optical). To confirm, the optical properties of the films before and after reductive annealing were probed by UV-vis spectroscopic ellipsometry.

The plots in Fig. 5(f) and (g) show the evolution of *k* as a function of the wavelength for Ru and Rh, respectively. In both cases, before annealing (after exposure at 841 J cm^{-2}), the film presents low values of *k*, especially at low wavelengths in the visible range that are attributed to the presence of colored Ru and Rh complexes in the films. After reductive annealing, the value of *k* drastically increased especially in the near-infrared region; this behavior is characteristic of the formation of metallic conducting films.

Conclusions

In conclusion, for the first time, we demonstrated that sol–gel processed mesostructured xerogels composed of noble metal precursors (Ru and Rh-based) act as negative tone resists for X-ray lithography. The effect of X-ray radiation on the structure and chemical composition of the films was investigated by a set of techniques including GISAXS, UV-vis and IR ellipsometry. Different from other sol–gel based materials, no condensation occurred but X-ray radiation induces the destructuration of the noble metal xerogels. We propose that the decomposition, dehydration and partial hydroxylation of the block-copolymer are responsible for the solubility switch observed in the xerogels. We demonstrate that noble metal xerogels be directly patterned by X-ray lithography and converted into the corresponding metals by annealing. The process presents several advantages: it enables direct patterning and minimizes expensive noble metal precursor waste. Notably, the development step was performed in water, a key requirement for recycling of the resist. In the present work, we demonstrated the fabrication of micrometric patterns, and the DXRL theoreti-

cally enables patterning at the sub-micrometric scale. We believe that this report will trigger new fundamental research on the X-ray assisted synthesis of nanostructured materials providing new possibilities for device fabrication at a low cost. From a fundamental point of view, this work expands the synthetic toolbox of sol–gel processed materials toward metals. We also provide a new understanding of the radiation chemistry of noble metal materials, a relatively underexplored field that is also of high interest for a broader community working on catalysis and electrocatalysis. As a future research line, it would be interesting to investigate if and how X-ray radiation influences the catalytic properties of noble metal films.

Conflicts of interest

There are no conflicts to declare.

Acknowledgements

This work was supported by French state funds managed by the National Research Agency (ANR) through the MetaFleSS project, Grant No. ANR-17-CE09-0027. M. F. acknowledges funding from the European Research Council (ERC) under European Union's Horizon 2020 Program (Grant Agreement no. 803220, TEMPORE). This project also received funding from the EU-H2020 research and innovation program under grant agreement no. 654360, having benefitted from the access provided to the DXRL and Austrian SAXS beamline at ELETTRA Trieste, Italy, within the framework of the NFFA-Europe Transnational Access Activity. The infrared ellipsometry was funded by the Région Ile-de-France in the framework of DIM ResPore and by the French state within the Investissements d'Avenir programme under the reference ANR-11-IDEX-0004-02, within the framework of the Cluster of Excellence MATISSE. The XPS KAlpha+ was funded by the Région Île-de-France (convention SESAME no. 16016303). ANR (Agence Nationale de la Recherche) and CGI (Commissariat à l'Investissement d'Avenir) are also gratefully acknowledged for their financial support through Labex SEAM (Science and Engineering for Advanced Materials and Devices), ANR-10-LABX-096 and ANR-18-IDEX-0001. We thank D. Montero and the Institut des Matériaux de Paris Centre (IMPC FR2482) for servicing the FEGSEM & EDX instrumentation, and Sorbonne Université, CNRS and C'Nano projects of the Région Ile-de-France for funding.

Notes and references

1 A. Mallavarapu, P. Ajay, C. Barrera and S. V. Sreenivasan, *ACS Appl. Mater. Interfaces*, 2021, **13**, 1169–1177.
2 M. Grobis, C. Schulze, M. Faustini, D. Grosso, O. Hellwig, D. Makarov and M. Albrecht, *Appl. Phys. Lett.*, 2011, 98.
3 H.-L. Chen, A. Cattoni, R. De Lépinau, A. W. Walker, O. Höhn, D. Lackner, G. Siefer, M. Faustini, N. Vandamme and J. Goffard, *Nat. Energy*, 2019, **4**, 761–767.
4 H.-I. Ryoo, J. S. Lee, C. B. Park and D.-P. Kim, *Lab Chip*, 2011, **11**, 378–380.
5 B. Jiang, C. Li, H. Qian, M. S. A. Hossain, V. Malgras and Y. Yamauchi, *Angew. Chem., Int. Ed.*, 2017, **56**, 7836–7841.
6 Y. Gutiérrez, R. Alcaraz de la Osa, D. Ortiz, J. M. Saiz, F. González and F. Moreno, *Appl. Sci.*, 2018, **8**, 64.
7 R. J. Seymour and J. O'Farrelly, *Kirk–Othmer Encyclopedia of Chemical Technology*, 2000, pp. 1–37, DOI: 10.1002/0471238961.1612012019052513.a01.pub3.
8 L. G. Wen, C. Adelmann, O. V. Pedreira, S. Dutta, M. Popovici, B. Briggs, N. Heylen, K. Vanstreels, C. J. Wilson, S. Van Elshocht and K. Croes, Ruthenium metallization for advanced interconnects, in *2016 IEEE International Interconnect Technology Conference/Advanced Metallization Conference (IITC/AMC)*, IEEE, pp. 34–36.
9 T. N. Arunagiri, Y. Zhang, O. Chyan, M. El-Bouanani, M. J. Kim, K. H. Chen, C. T. Wu and L. C. Chen, *Appl. Phys. Lett.*, 2005, **86**, 083104.
10 A. M. Watson, X. Zhang, R. Alcaraz de la Osa, J. M. Sanz, F. González, F. Moreno, G. Finkelstein, J. Liu and H. O. Everitt, *Nano Lett.*, 2015, **15**, 1095–1100.
11 O. Dalstein, D. R. Ceratti, C. Boissière, D. Grosso, A. Cattoni and M. Faustini, *Adv. Funct. Mater.*, 2016, **26**, 81–90.
12 M. Tu, B. Xia, D. E. Kravchenko, M. L. Tietze, A. J. Cruz, I. Stassen, T. Hauffman, J. Teyssandier, S. De Feyter and Z. Wang, *Nat. Mater.*, 2021, **20**, 93–99.
13 M. Faustini, *Nat. Mater.*, 2021, **20**, 8–9.
14 O. Dalstein, E. Gkaniatsou, C. Sicard, O. Sel, H. Perrot, C. Serre, C. Boissière and M. Faustini, *Angew. Chem., Int. Ed.*, 2017, **56**, 14011–14015.
15 A. Cattoni, D. Mailly, O. Dalstein, M. Faustini, G. Seniutinas, B. Rösner and C. David, *Microelectron. Eng.*, 2018, **193**, 18–22.
16 M. Faustini, C. Boissiere, L. Nicole and D. Grosso, *Chem. Mater.*, 2014, **26**, 709–723.
17 M. Faustini, M. Vayer, B. Marmiroli, M. Hillmyer, H. Amenitsch, C. Sinturel and D. Grosso, *Chem. Mater.*, 2010, **22**, 5687–5694.
18 M. Faustini, B. Marmiroli, L. Malfatti, B. Louis, N. Krins, P. Falcaro, G. Grenci, C. Laberty-Robert, H. Amenitsch, P. Innocenzi and D. Grosso, *J. Mater. Chem.*, 2011, **21**, 3597–3603.
19 P. Falcaro, L. Malfatti, L. Vaccari, H. Amenitsch, B. Marmiroli, G. Grenci and P. Innocenzi, *Adv. Mater.*, 2009, **21**, 4932–4936.
20 L. Malfatti, D. Marongiu, S. Costacurta, P. Falcaro, H. Amenitsch, B. Marmiroli, G. Grenci, M. F. Casula and P. Innocenzi, *Chem. Mater.*, 2010, **22**, 2132–2137.
21 D. R. Ceratti, B. Louis, X. Paquez, M. Faustini and D. Grosso, *Adv. Mater.*, 2015, **27**, 4958–4962.
22 P. Innocenzi, T. Kidchob, S. Costacurta, P. Falcaro, B. Marmiroli, F. Cacho-Nerin and H. Amenitsch, *Soft Matter*, 2010, **6**, 3172–3176.
23 M. Gayrard, J. Voronkoff, C. Boissière, D. Montero, L. Rozes, A. Cattoni, J. Peron and M. Faustini, *Nano Lett.*, 2021, **21**(5), 2310–2317.

24 S. Duran, M. Elmaalouf, M. Odziomek, J.-Y. Piquemal, M. Faustini, M. Giraud, J. Peron and C. Tard, *ChemElectroChem*, 2021, **8**, 3519–3524.
25 M. Odziomek, M. Bahri, C. Boissière, C. Sanchez, B. Lassalle-Kaiser, A. Zitolo, O. Ersen, S. Nowak, C. Tard, M. Giraud, M. Faustini and J. Peron, *Mater. Horiz.*, 2020, **7**(2), 541–550.
26 R. M. Silverstein and G. C. Bassler, *J. Chem. Educ.*, 1962, **39**, 546.
27 K. Pielichowski and K. Flejtuch, *J. Anal. Appl. Pyrolysis*, 2005, **73**, 131–138.
28 P. Innocenzi, L. Malfatti and P. Falcaro, *Soft Matter*, 2012, **8**, 3722–3729.
29 I. Povar and O. Spinu, *J. Electrochem. Sci. Eng.*, 2016, **6**, 145–153.